

Interface learning of multiphysics and multiscale systems

Shady E. Ahmed, Omer San,* and Kursat Kara

School of Mechanical & Aerospace Engineering, Oklahoma State University, Stillwater, OK 74078, USA.

Rami Younis

*The McDougall School of Petroleum Engineering,
The University of Tulsa, Tulsa, OK 74104, USA.*

Adil Rasheed

Department of Engineering Cybernetics, Norwegian University of Science and Technology, N-7465, Trondheim, Norway.

(Dated: June 9, 2022)

Complex natural or engineered systems comprise multiple characteristic scales, multiple spatiotemporal domains, and even multiple physical closure laws. To address such challenges, we introduce an interface learning paradigm and put forth a data-driven closure approach based on memory embedding to provide physically correct boundary conditions at the interface. Our findings in solving a bi-zonal nonlinear advection-diffusion equation show the proposed approach's promise for multiphysics and multiscale systems. We also highlight that high-performance computing environments can benefit from this methodology to reduce communication costs among processing units in emerging machine learning ready heterogeneous platforms toward exascale era.

Numerical simulations of multiscale, multicomponent, multiphysics and multidisciplinary systems require proper treatment of interface boundary conditions among solvers. Otherwise, in a naive implementation, the stiffest part of the domain dictates the overall spatial mesh resolution and time stepping requirements, making such simulations computationally daunting. Most of such problems that incorporate some sort of information share can be put into the following six categories, explained with examples as follows:

1. FOM-ROM coupling: With the emergence of digital twin like technologies, there is a demand for lighter models that can run in real time [1, 2]. In the context of weather prediction, the full order model (FOM) has been in use for a long time; however, they are incapable of modelling phenomena associated with scales smaller than what the coarse mesh can handle (like buildings and small terrain variations). These fine scale flow structures can be modelled using a much refined mesh but then the simulations become computationally intractable. To tackle this problem a large variety of reduced order models (ROMs) are being developed. In order to make these ROMs realistic there is a need to couple them to FOM model so that the FOM provides the interface conditions (both in space and time) to the ROM.

2. Multiphysics and multiscale coupling: Various flow dichotomies with a multiphysics coupling of interacting subsystems can be identified in a gas turbine flow. The rotating parts and wall turbulence largely govern the flow within the compressor and turbine sections. On the other hand, for the flow within the combustor, chemical reactions, heat release, acoustics, and the presence of fuel spray come into play. Thus, a simulation of the flow

within the combustion chamber is significantly more expensive and demanding than other sections. It would require a finer and more sophisticated mesh, smaller time step, and less numerical simplifications. Therefore, using a unified global solver for the whole system would be either too expensive (matching the level of the fidelity required for the expensive part), or unacceptably inaccurate (following the level of fidelity required for the inexpensive part). Instead, multiple solvers are usually utilized to address different parts [3, 4], and information is transferred between solvers.

3. Geometric multiscale: Blood flow in the whole circulatory system is mathematically described by means of heterogeneous problems featuring different degree of detail and different geometric dimension that interact together through appropriate interface coupling conditions. Proper exchange of interface conditions between models operating at different geometric approximations open altogether new vistas for biofluids simulations [5–7].

4. Model fusion: Turbulence modelling generally requires an apriori selection of the most suited model to handle a particular kind of flow. However, it is seldom that one model is sufficient for different kind of zones in the computational domain. To alleviate this problem, hybrid and blending models have been extensively utilized to lift technical barriers in industrial applications, especially in settings where the Reynolds-averaged Navier-Stokes (RANS) approach is not sufficient and large eddy simulation (LES) is expensive [8–10]. The approach can be extended to blend any number of turbulence models provided the exchange of information at the interface can be accurately modelled [11].

5. Nested solvers: To decrease the computational cost required for an accurate representation of the numerous interconnected physical systems, e.g., oceanic and atmospheric flows, several classes of nested models have been developed and form the basis of highly successful appli-

* osan@okstate.edu

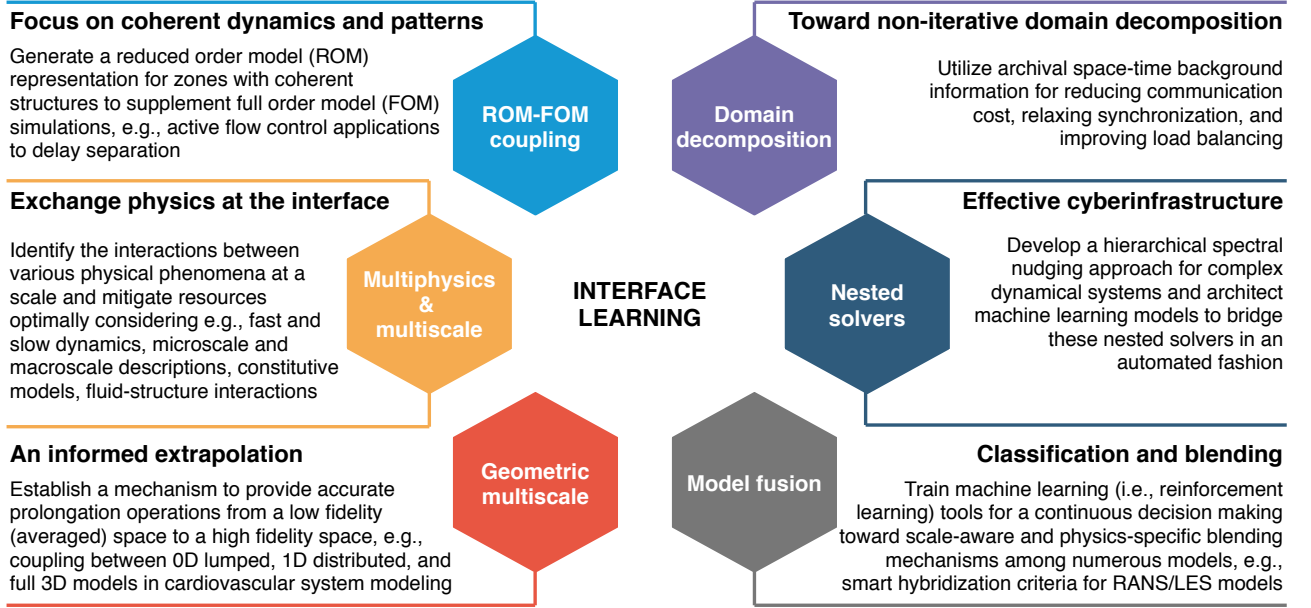


FIG. 1. Big picture of the interface learning paradigm considering numerous scientific and engineering interpretations.

cations and research at numerous weather and climate centers. Enforcing consistent flow conditions between successive nesting levels is also considered one form of interface matching. For example, a spectral nudging approach has been successfully implemented to force the large-scale atmospheric states from global climate models onto a regional climate model [12–17].

6. Domain decomposition: Since various zones in multiscale systems are connected through interfaces, data sharing, and communicating consistent interface boundary conditions among respective solvers are inevitable. Likewise, multirate and locally adaptive stepping methods can yield a mismatch at the space-time interface, and simple interpolation or extrapolation might lead to solution divergence or instabilities [18]. An analogous situation usually occurs in parallel computing environments with domain decomposition and distribution over separate processors with message passing interface to communicate information between processors. The heterogeneity of different processing units creates an asynchronous computational environment, and the slowest processors will control the computational speed unless load-balancing is performed [19, 20].

In short we can conclude that developing novel methodologies to model the information exchange at the interface will have far reaching impact on a large variety of problems as shown in Fig. 1. To this end, the current letter puts forth an approach based on memory embedding via machine learning to provide physically correct interfacial conditions. In particular, the proposed technique relies on the time history of local information to estimate consistent boundary conditions at the sub-domain boundaries without the need to resolve the neighboring regions (on the other side of the interface). It enables

us to focus our computational resources on the region or scales of interest. The proof-of-concept computations on a bi-zonal one-dimensional Burgers’ problem showcase the proposed approach’s promise for stiff multiscale systems. We also highlight that high-performance computing environments can benefit from this methodology to reduce communication costs among processing units.

Two-component system — As a demonstration of interface learning, we consider an application to the one-dimensional (1D) viscous Burgers problem. It combines the effects of viscous diffusion, friction, and nonlinear advection, and thus serves as a prototypical test bed for several numerical simulations studies. In order to mimic multiscale/multiphysics systems, we suppose the domain consists of two distinguishable zones corresponding to different physical parameters as follows,

$$\frac{\partial u}{\partial t} + u \frac{\partial u}{\partial x} = \nu \frac{\partial^2 u}{\partial x^2} - \gamma u, \quad (1)$$

$$(\nu, \gamma) = \begin{cases} (10^{-2}, 0) & \text{for } 0 \leq x \leq x_b \\ (10^{-4}, 1) & \text{for } x_b < x \leq 1, \end{cases} \quad (2)$$

where x_b is the spatial location of the interface. In a naive implementation, a numerical solution of this problem would imply the use of a grid resolution and time step corresponding to the stiffest part (i.e., the left part in this case), all over the domain unless we adopt an implicit scheme which is unconditionally stable but requires a nonlinear solver typically at each time step. Certainly, this puts an excessive and unnecessary computational burden. For example, if we opt to using a spatial resolution of 4096 grid spacings with a simple forward in time central in space (FTCS) scheme, the maximum time step that can be used in the left zone is approximately

2.5×10^{-6} (i.e., $\delta t \leq \delta x^2/(2\nu)$ based on von Neumann stability analysis). Instead, the right zone gives the flexibility of using a 100 times larger time step. However, resolving the whole domain simultaneously would dictate the smaller time step, even if we are only interested in the right zone. A similar scenario would take place in multi-component systems with varying spatial grid resolutions, where a unified resolution all over the domain becomes unpractical. Thus, we explore the introduction of a memory embedding architecture to enable resolving the zone of interest independently of the rest of the domain.

Memory embedding of interface boundaries — For machine learning applicability, a pattern must exist and most fluid flows are dominated by coherent structures. Thus, our underlying hypothesis is the existence of a dynamical context or correlation between the past values of flow features at the interface and its one-sided neighbors (i.e., $u(x_b, t_n)$, $u(x_b + \delta x, t_n)$, $u(x_b + 2\delta x, t_n)$, \dots), and the future state at the interface (i.e., $u(x_b, t_n + \delta t)$). This corresponds to the *Learn from Past* (LP) model in Fig. 2. Since we incorporate a fully explicit time stepping scheme in our simulation, the interface neighboring points might be evolved in time before the interface condition is updated. Thus, a variant of the LP model based on a combination between old and updated values, namely the *Learn from Past and Present* (LPP) model, can be utilized as well. Furthermore, we extend this mapping to take into account the time history dependence in a non-Markovian manner through the adoption of recurrent neural networks. Those exploit an internal state feature that reserves information from past input to learn the *context* to improve and refine the output. For the neural network architecture, we use a simplistic long short-term memory (LSTM) of two layers, 20 neurons each. Although more sophisticated ML architectures and/or numerical schemes (e.g., [21–24]) might be utilized, the main objective of the present study is to emphasize the potential of neural networks to advance computational fluid dynamics (CFD) simulations for multiscale and multicomponent systems.

Proof-of-concept results — For the demonstration and assessment of the introduced methodology of interface learning, we consider two examples of varying complexity. In the first example, we address the problem of a travelling square wave, where the initial condition is defined with an amplitude of 1 in the left zone (i.e., $0 \leq x \leq x_b$), and zero in the right zone. In other words, the interface is exactly placed at the discontinuity location of the initial propagating wave. So, the wave is guaranteed to instantaneously enter the right zone once the flow is triggered. In a second example of increasing complexity, we study the evolution of a pulse wave completely contained in a portion of the left region. The initiation of flow dynamics in the truncated domain is controlled by the interplay between advection, diffusion, and friction in different regions. For both examples, we solve the presented viscous 1D Burgers problem for a time span of $[0, 1]$ using a time step of 2.5×10^{-6} to resolve the whole domain $x \in [0, 1]$

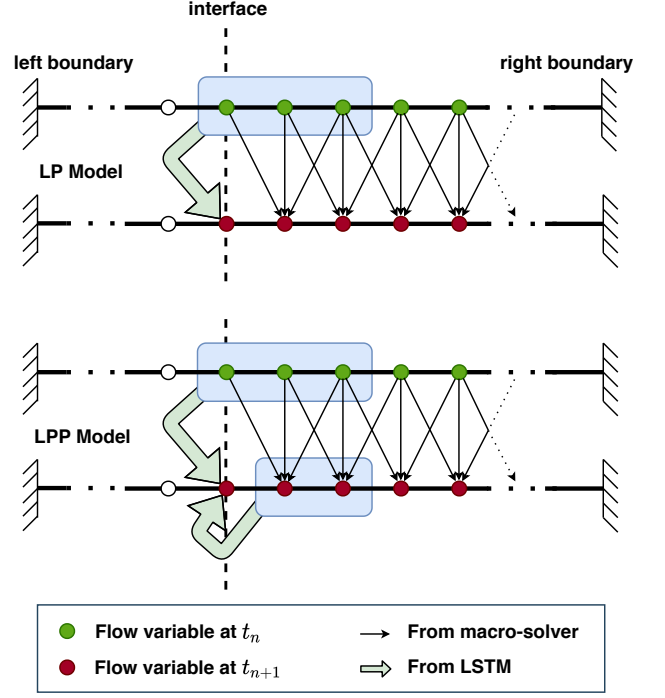


FIG. 2. Different models to utilize LSTM mapping for learning boundary conditions at interface

over a spatial grid resolution of 4096. For external boundary conditions, we assume zero Dirichlet boundary conditions (i.e., $u(0, t) = u(1, t) = 0$). Data snapshots are stored every 100 time steps (corresponding to the coarse time step of 2.5×10^{-4}).

For interface learning, we consider two schemes/models for the training as illustrated in Fig. 2 to learn the dynamics at the internal boundary separating the two compartments of different physical properties. For testing, we consider the truncated 1D domain, where $x_b \leq x \leq 1$, and resolve the flow dynamics in this portion using a coarse time step of 2.5×10^{-4} , thus denoted the macro-solver here. We adopt the LSTM learning to update the left boundary condition (i.e., at $x = x_b$). For the right boundary (i.e., at $x = 1$), we keep the global zero Dirichlet conditions.

Example 1: travelling square wave. In this example, we consider the following initial condition,

$$u(x, 0) = \begin{cases} 1 & \text{for } 0 \leq x \leq x_b \\ 0 & \text{for } x_b < x \leq 1. \end{cases} \quad (3)$$

In particular, we generate data for $x_b \in \{1/8, 2/8, 3/8, 4/8, 5/8, 6/8, 7/8\}$, and we use field data at $x_b \in \{1/8, 3/8, 5/8, 7/8\}$ for training and reserve the remaining cases for the out-of-sample testing. To enhance the neural network performance, we augment the input vector with the spatial and temporal information as well. In other words, LP Model can be interpreted as the mapping $u(x_b, t_n + \delta t) = G_1(u(x_b, t_n), u(x_b + \delta x, t_n), u(x_b + 2\delta x, t_n), \dots, x_b, x_b + \delta x, x_b + 2\delta x, \dots, t_n)$,

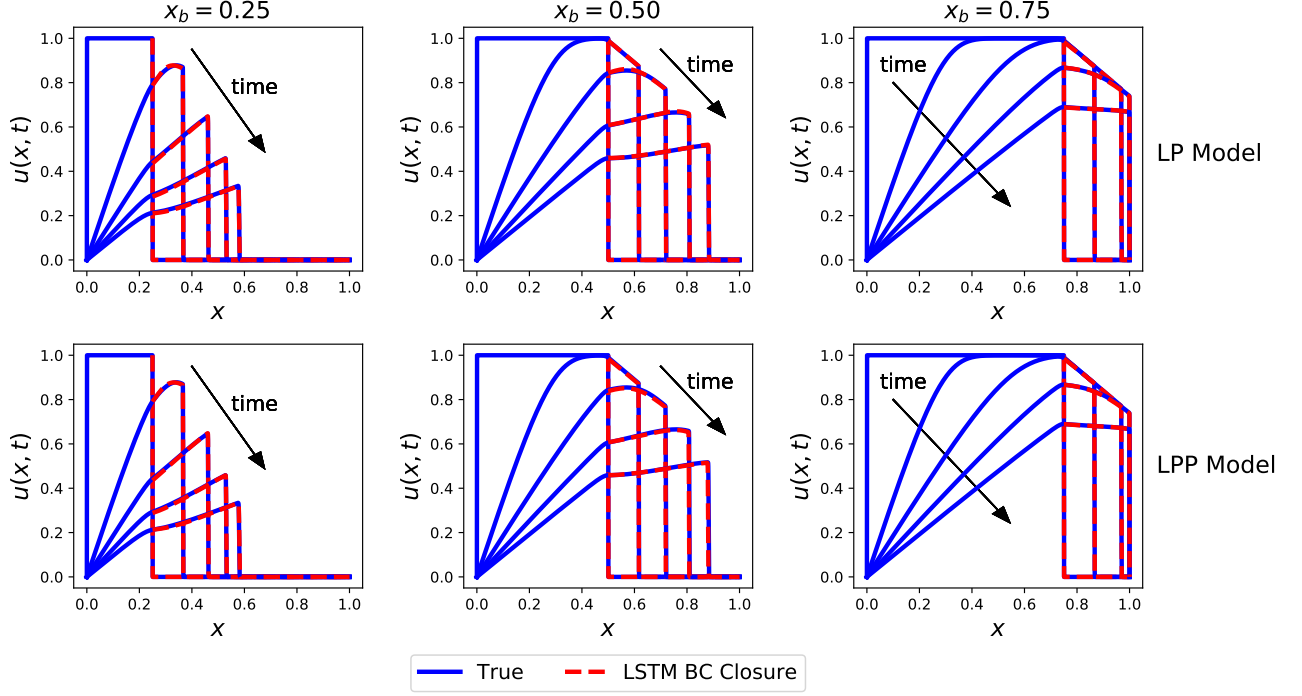


FIG. 3. Results for LSTM boundary condition closure for different values of x_b . Predicted velocity fields are shown at $t \in \{0.0, 0.25, 0.50, 0.75, 1.0\}$.

while LPP Model learns the map of $u(x_b, t_n + \delta t) = G_2(u(x_b, t_n), u(x_b + \delta x, t_n), u(x_b + 2\delta x, t_n), \dots, u(x_b + \delta x, t_n + \delta t), u(x_b + 2\delta x, t_n + \delta t), \dots, x_b, x_b + \delta x, x_b + 2\delta x, \dots, t_n, t_n + \delta t)$.

We compare the predicted velocity field within the truncated domain using the proposed LSTM boundary condition (BC) closure approach with respect to the true solution obtained by solving the whole domain. We note here that the LSTM BC closure results are based on utilizing the macro-solver (i.e., using a time step of 2.5×10^{-4}), while the true solution is obtained by adopting the micro-solver (i.e., using a time step of 2.5×10^{-6}). The spatio-temporal evolution of the velocity field for $x_b \in \{1/4, 2/4, 3/4\}$ is shown in Fig. 3, where x_b is the location of the interface. We note that Fig. 3 corresponds to a three-point stencil for the LSTM mapping. In other words, the LP model uses values of $u(x_b, t_n)$, $u(x_b + \delta x, t_n)$, and $u(x_b + 2\delta x, t_n)$ for the prediction of $u(x_b, t_n + \delta t)$, while the LPP model uses $u(x_b, t_n)$, $u(x_b + \delta x, t_n)$, $u(x_b + 2\delta x, t_n)$, $u(x_b + \delta x, t_n + \delta t)$, and $u(x_b + 2\delta x, t_n + \delta t)$. Visual results advocate the capability of the presented approach of predicting accurate values for the interface boundary condition at different times. For more quantitative assessment, we also compute the resulting root mean-squares error (RMSE) defined as

$$\text{RMSE} = \sqrt{\frac{1}{N_t N_x} \sum_{n=1}^{N_t} \sum_{i=1}^{N_x} (u^T(x_i, t_n) - u^P(x_i, t_n))^2}, \quad (4)$$

where u^T is the true velocity field, and u^P represents the predictions by the LSTM BC closure approach. In the above formula, N_x stands for the number of grid points involved only in the truncated domain. In other words, it considers only the flow field values within $[x_b, 1]$.

The RMSE values of the LSTM BC closure predictions using a two- and three-point stencils are documented in Table I using the LP and LPP models. Quantitative results imply that the LP model is giving slightly better results than the LPP model. We believe that this behavior is because the LP model is more consistent with the adopted FTCS numerical scheme, where the time evolution relies explicitly on the *old* values of the flow fields. Moreover, this might be attributed to the sub-optimal architecture we use for the LSTM. Although we found that results are not very sensitive to the given *hyperparameters*, further tuning might be required to provide *optimal* performance. We also see from Table I that an increase in the stencil size from 2 to 3 improves results. Nonetheless, a 2-point stencil mapping still provides acceptable predictions, confirming the validity and robustness of the LSTM memory embedding skills to yield physically consistent and accurate state estimates at the interface using local information, and may hold immense potential for designing ML-ready predictive engines in physical sciences.

Example 2: pulse problem. In this case, we consider an initial condition of a pulse, completely contained in the left region and study its propagation and travel from the left to right compartments. In particular, the initial

TABLE I. RMSE of LSTM boundary condition closure results using different models with two-point and three-point mapping.

x_b	LP Model		LPP Model	
	2 Points	3 Points	2 Points	3 Points
0.125	1.5×10^{-2}	2.9×10^{-3}	2.6×10^{-2}	1.4×10^{-2}
0.250	4.4×10^{-2}	3.5×10^{-3}	2.8×10^{-2}	3.4×10^{-3}
0.375	8.4×10^{-3}	3.6×10^{-3}	2.0×10^{-2}	1.6×10^{-2}
0.500	2.9×10^{-2}	2.6×10^{-3}	1.7×10^{-2}	2.3×10^{-2}
0.625	6.4×10^{-3}	3.7×10^{-3}	1.9×10^{-2}	1.3×10^{-2}
0.750	1.0×10^{-2}	5.4×10^{-3}	1.2×10^{-2}	1.7×10^{-3}
0.875	2.1×10^{-3}	1.8×10^{-3}	6.7×10^{-3}	4.4×10^{-3}

pulse can be represented as

$$u(x, 0) = \begin{cases} 1 & \text{for } 0 \leq x \leq w_p \\ 0 & \text{for } w_p < x \leq 1, \end{cases} \quad (5)$$

where w_p is the pulse width. For illustration, we store results corresponding to 7 varying pulse widths as $w_p \in \{0.20, 0.21, 0.22, 0.23, 0.24, 0.25, 0.26\}$. We use $w_p \in \{0.20, 0.22, 0.24, 0.26\}$ for training and validation, while we assign $w_p \in \{0.21, 0.23, 0.25\}$ for out-of-sample testing. For interface, we consider a fixed interface location at $x_b = 0.3$ (i.e., on the right of the largest pulse width). This is to let the interplay between the different interacting mechanisms (i.e., advection, diffusion, and friction) to come into effect *before* the pulse travels into the truncated zone. Thus the state at the interface is more dependent on the flow dynamics in *both* domain partitions. Since the pulse width is a key factor in this problem setting, we augment our input vector with w_p as well. For this particular example, we found that enforcing higher memory embedding is crucial in providing accurate results. Specifically, we adopt a sliding window of a three-time step history (also called a lookback of 3) in our LSTM implementation. Results for the LP and LPP schemes are shown in Fig. 4 using 3-point mapping. We find that both schemes can sufficiently learn the interface dynamics and accurately predict its condition at out-of-sample settings.

In Table II, we report the RMSE obtained from the interface learning approach using the LP and LPP schemes for the 1D pulse problem described above. We can see that memory embedding for interface learning yields very accurate results for truncated domain computations. Results in this table include those obtained from both in-sample and out-of-sample data. However, we highlight here that even the in-sample training and testing are substantially different. During the training phase, the LSTM is always fed with true inputs obtained from the micro-solver applied over the whole domain. In contrast, for testing, the LSTM only sees the *true* state at initial time. After that, the output of the LSTM is provided to the macro-solver to evolve in time, and the evolved states are then given to the LSTM as new input. This recursive deployment can introduce numerical noise as a result of

the temporal advancement with larger time-step as well as uncertainties at interface conditions.

TABLE II. RMSE of LSTM boundary condition closure for the pulse example using different models with two-point and three-point stencils.

w_p	LP Model		LPP Model	
	2 Points	3 Points	2 Points	3 Points
0.20	2.6×10^{-2}	8.6×10^{-3}	2.6×10^{-2}	1.1×10^{-2}
0.21	3.0×10^{-2}	6.5×10^{-3}	3.2×10^{-2}	1.7×10^{-3}
0.22	2.7×10^{-2}	3.9×10^{-3}	3.4×10^{-2}	1.4×10^{-2}
0.23	1.8×10^{-2}	3.5×10^{-3}	3.5×10^{-2}	2.0×10^{-2}
0.24	7.1×10^{-3}	4.4×10^{-3}	3.4×10^{-2}	1.4×10^{-2}
0.25	8.7×10^{-3}	5.7×10^{-3}	2.9×10^{-2}	1.0×10^{-2}
0.26	1.6×10^{-2}	5.6×10^{-3}	2.6×10^{-2}	1.2×10^{-2}

Conclusions — In this work, we have demonstrated the potential of machine learning tools to advance and facilitate CFD simulations of multiscale, multicomponent systems. In particular, we have shown the capability of memory embedding to learn the dynamics at the interface between different zones. This is especially beneficial where the domain contains zones with strong dynamics and components with complex configuration that might dictate a very fine mesh resolutions and time stepping. The proposed approach enables us to focus our efforts onto the domain portion of interest, while satisfying physically consistent interface conditions. It can serve as a non-iterative domain decomposition method. Toward model fusion technologies, such an interface learning methodology might also hold significant promise for the development of blending criteria in hybrid RANS/LES models. A proof-of-concept has been demonstrated using the 1D viscous Burgers equation over a two-zone domain with different physical parameters. An LSTM is used to bypass the micro-solver corresponding the stiff region and provide valid interface boundary conditions to enable the macro-solver to run independently. We have illustrated the success and robustness of the proposed methodology using different learning configurations. Both LP and LPP models are the key concepts introduced in this letter, especially for designing intelligent boundary closure schemes, which may bear huge potential in many scientific disciplines. Finally, we emphasize that a similar interface closure technique can be adopted in high performance computing environments, to minimize the communication cost and delay between different asynchronous processors, a topic we would like to pursue further in the future.

This material is based upon work supported by the U.S. Department of Energy, Office of Science, Office of Advanced Scientific Computing Research under Award Number DE-SC0019290. O.S. gratefully acknowledges their support.

The data that support the findings of this study are available from the corresponding author upon request.

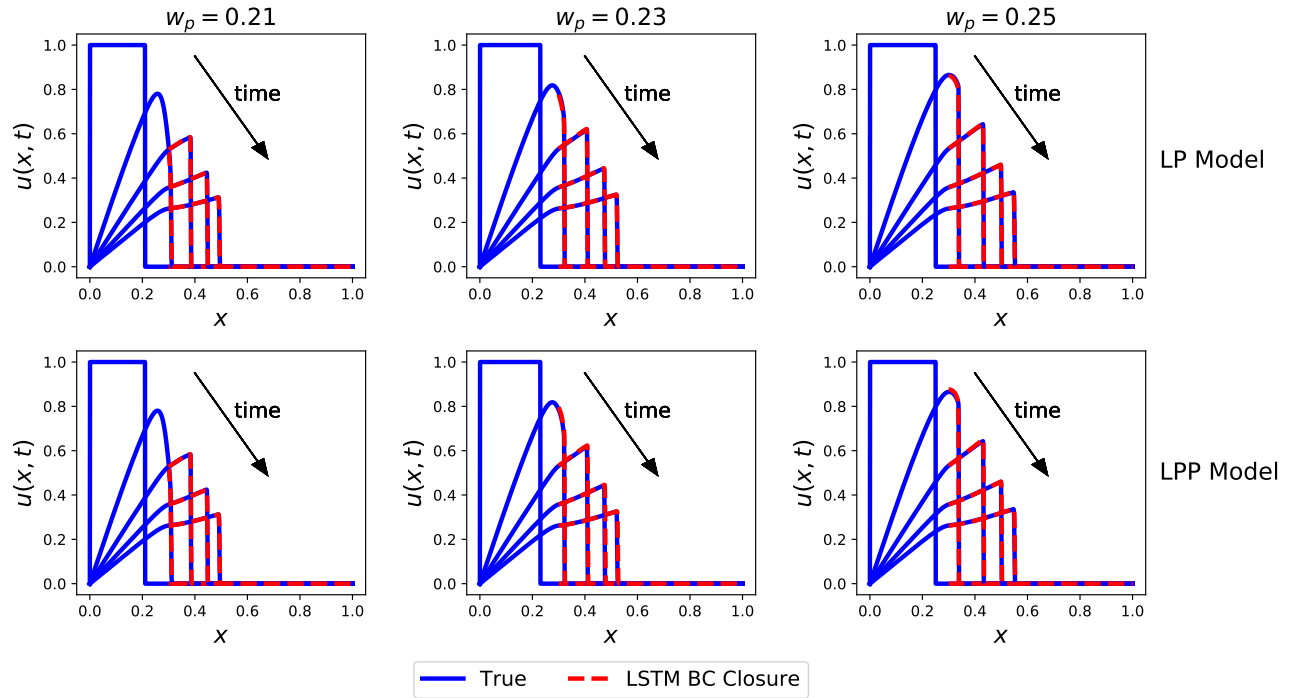


FIG. 4. Results for LSTM boundary condition closure for the pulse problem using different values of w_p . Predicted velocity fields are shown at $t \in \{0.0, 0.25, 0.50, 0.75, 1.0\}$.

-
- [1] B. Peherstorfer, K. Willcox, and M. Gunzburger, *SIAM Review* **60**, 550 (2018).
 - [2] F. Naets, D. De Gregoriis, and W. Desmet, *International Journal for Numerical Methods in Engineering* **118**, 765 (2019).
 - [3] S. Shankaran, J. Alonso, M.-F. Liou, N.-S. Liu, and R. Davis, in *39th Aerospace Sciences Meeting and Exhibit* (2001) p. 974.
 - [4] J. Xu, C. Huang, and K. Duraisamy, *AIAA Journal* **58**, 618 (2020).
 - [5] A. Quarteroni and A. Veneziani, *Multiscale Modeling & Simulation* **1**, 173 (2003).
 - [6] T. Passerini, M. De Luca, L. Formaggia, A. Quarteroni, and A. Veneziani, *Journal of Engineering Mathematics* **64**, 319 (2009).
 - [7] A. Quarteroni, A. Veneziani, and C. Vergara, *Computer Methods in Applied Mechanics and Engineering* **302**, 193 (2016).
 - [8] P. Sagaut, *Multiscale and multiresolution approaches in turbulence: LES, DES and hybrid RANS/LES methods: applications and guidelines* (Imperial College Press, Danvers, MA, USA, 2013).
 - [9] A. Fadaei-Ghotbi, C. Friess, R. Manceau, and J. Borée, *Physics of Fluids* **22**, 055104 (2010).
 - [10] M. L. Shur, P. R. Spalart, M. K. Strelets, and A. K. Travin, *International Journal of Heat and Fluid Flow* **29**, 1638 (2008).
 - [11] R. Maulik, O. San, J. D. Jacob, and C. Crick, *Journal of Fluid Mechanics* **870**, 784 (2019).
 - [12] K. M. Waldron, J. Paegle, and J. D. Horel, *Monthly Weather Review* **124**, 529 (1996).
 - [13] H. von Storch, H. Langenberg, and F. Feser, *Monthly Weather Review* **128**, 3664 (2000).
 - [14] R. Radu, M. Déqué, and S. Somot, *Tellus A: Dynamic Meteorology and Oceanography* **60**, 898 (2008).
 - [15] G. Miguez-Macho, G. L. Stenchikov, and A. Robock, *Journal of Geophysical Research: Atmospheres* **109** (2004).
 - [16] B. Rockel, C. L. Castro, R. A. Pielke Sr, H. von Storch, and G. Leoncini, *Journal of Geophysical Research: Atmospheres* **113** (2008).
 - [17] M. Schubert-Frisius, F. Feser, H. von Storch, and S. Rast, *Monthly Weather Review* **145**, 909 (2017).
 - [18] M. J. Gander and L. Halpern, in *Domain Decomposition Methods in Science and Engineering XX* (Springer, 2013) pp. 377–385.
 - [19] D. A. Donzis and K. Aditya, *Journal of Computational Physics* **274**, 370 (2014).
 - [20] A. Mittal and S. Girimaji, *Physical Review E* **96**, 033304 (2017).
 - [21] A. Rasheed, O. San, and T. Kvamsdal, *IEEE Access* **8**, 21980 (2020).
 - [22] A. Bowers, L. Rebholz, A. Takhirov, and C. Trenchea, *International Journal for Numerical Methods in Fluids* **70**, 805 (2012).
 - [23] C. C. Manica, M. Neda, M. Olshanskii, and L. G. Rebholz, *ESAIM: Mathematical Modelling and Numerical Analysis* **45**, 277 (2011).
 - [24] J. Borggaard and T. Iliescu, *Applied Mathematics Letters* **19**, 735 (2006).